


## Exact solutions for non-Rayleigh nondiffracting speckles

José G. M. N. Neto , Eduardo J. S. Fonseca, and Alcenísio J. Jesus-Silva 

*Instituto de Física, Universidade Federal de Alagoas, P.O. Box 2051, Maceió, Alagoas 57061-970, Brazil*

 (Received 13 May 2022; revised 3 October 2022; accepted 4 November 2022; published 28 November 2022)

We report on a speckle field that is non-Rayleigh, nondiffracting, and an exact solution to the scalar Helmholtz equation. We have shown that these fields can be directly optimized to a continuous range of contrast values corresponding to the sub-Rayleigh or super-Rayleigh statistics maintaining its nondiffracting characteristics. Besides, this work extends the range of non-Rayleigh statistics of nondiffracting fields, which may find many applications in the areas of solid-state physics, cold atoms, and optical imaging.

DOI: [10.1103/PhysRevA.106.053519](https://doi.org/10.1103/PhysRevA.106.053519)

Generally, scattering of coherent light by a disordered media generates speckles exhibiting Rayleigh statistics. This type of speckles is the result of the interference of a large number of independent partial waves with relative phases uniformly distributed in the range of  $2\pi$ , with its intensity presenting a negative exponential probability density function (PDF) [1]. Rayleigh speckles possess interesting properties like some healing capabilities [2], similar to the self-healing property [3,4] of Bessel beams [5], which enable them to image multiple superimposed planes in a scattering sample [6].

Non-Rayleigh speckle statistics can be artificially produced by appropriately encoding high-order correlations in the phase front of a monochromatic laser beam with a spatial light modulator (SLM) [7–10], and maintaining the properties of being fully developed, ergodic, and stationary [11]. The only limitation is that the non-Rayleigh statistics exists only in the plane of optimization; after a small distance of propagation the statistics revert back to Rayleigh statistics. Interestingly enough, optimized non-Rayleigh speckles are used for improving optical performance of microscope systems [12] and for ghost imaging [13,14].

A step forward was done by Ref. [15]. The authors proposed a method to generate non-Rayleigh nondiffracting (NRND) speckle fields. Nondiffracting fields have the wave vectors restricted to a diffraction cone, and their transversal profile does not change along the propagation [16]. In this case, the speckles are non-Rayleigh along a distance corresponding to several Rayleigh ranges, where the Rayleigh range (see Appendix B) is defined as the longitudinal length of a single grain of a diffracting speckle field of the same transverse grain length as the nondiffracting one [9]. These particular speckles are promising for applications such as generating a random potential for studies of disordered systems using cold atoms [17], designing new materials using a random potential created by shining light over colloidal systems [18], and exploring Anderson localization studies [19]. Nonetheless, the speckles of Ref. [15] also present limitations because the working principle relies on a spatial filtering by a

circular slit. Therefore, they can generate only speckles that can be filtered by the circular slit, i.e., the super-Rayleigh speckles with contrasts corresponding to an odd-powered transformation on the NRND speckles with contrast  $C = \sqrt{2}$ .

In this work we propose a method to directly generate a continuous range of intensity contrast values corresponding to the sub-Rayleigh and super-Rayleigh statistics and that is an exact solution of the scalar Helmholtz equation (HE). Therefore, we combine the robustness of speckles, the non-diffractive property, and the non-Rayleigh statistics, boosting the power for imaging applications, solid-state physics, and cold atoms; for example, enabling an extended depth of focus and circumventing the optical diffraction limit [12].

In order to calculate the exact non-Rayleigh nondiffracting (ENRND) speckle fields, we start with the solution of the HE represented by the Whittaker integral [20,21],

$$U(x, y, z) = e^{-ik_z z} \int_0^{2\pi} \Phi(\phi) e^{-ik_t(x \cos \phi + y \sin \phi)} d\phi, \quad (1)$$

where  $\Phi(\phi)$  can be an arbitrary function,  $k_z = \sqrt{k^2 - k_t^2}$ ,  $k = 2\pi/\lambda$ ,  $k_x = k_t \cos \phi$ ,  $k_y = k_t \sin \phi$ , and  $\lambda$  is the wavelength of the light.

Now, we consider the discrete form of Eq. (1), that can be written as [22]

$$U(x, y, z) = \frac{2\pi}{Q-1} e^{-ik_z z} \sum_n \Phi(\phi_n) e^{-ik_t(x \cos \phi_n + y \sin \phi_n)}, \quad (2)$$

where  $\phi_n = 2n\pi/(Q-1)$  and  $n = 0, \dots, Q-1$ .

For the generation of the ENRND speckle fields we choose  $\Phi(\phi_n) = \exp[i\theta(\phi_n)]$ , where  $\theta(\phi_n)$  must be appropriately optimized ensuring that it is still an element of a random phase array with phase values uniformly distributed over  $[0, 2\pi]$ . Figure 1 illustrates the principle of the algorithm. The main idea is to write  $\theta$  as the sum of two random uniformly distributed phase arrays  $A$  and  $B$ ,  $\theta = A + B$ , both with length  $Q$ . We use a third random uniformly distributed phase array  $D$ , which is composed of  $N \leq Q$  elements. In each iteration we sequentially select the elements of  $D$  and substitute it in a randomly selected position of  $A$  and calculate the corresponding contrast  $C = \sqrt{\langle I^2 \rangle / \langle I \rangle^2 - 1}$ , where  $I = |U|^2$  is the intensity.

\*alcenisio@fis.ufal.br

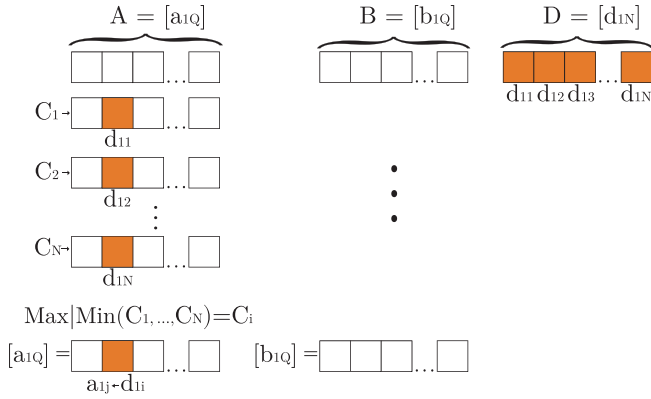


FIG. 1. Diagram that represents one iteration of the algorithm. We have two arrays  $A$  and  $B$  with one line and  $Q$  columns. The arrays have random elements uniformly distributed over  $[0, 2\pi]$ . Also, array  $D$  has one line and  $N$  columns with  $N \leq Q$ , and the elements have the same properties as the other arrays.

After that, we select the new  $A$  that have the biggest or smaller contrast according to if we want to maximize or minimize the contrast. As indicated in Fig. 1, we randomly select a single position and we maintain it during each iteration. We proceed to the next iteration repeating the same process until reaching the desired contrast. After each iteration the phase  $D$  is updated with new random values, ensuring uniform convergence even when  $N$  is as small as  $N = Q/4$  and, therefore, speeding up the calculation (see Appendix C). The array  $B$  remains unchanged along the optimization. In summary, in each iteration we choose a new  $A$  with one updated entry. That new  $A$  generates the maximum/minimum contrast between the  $N$  samples produced during one iteration.

The role of the array  $B$  is to ensure that the speckle pattern is fully developed after optimization. The reasoning behind the algorithm—how it produces spatial correlations between the phase values of  $\theta$ —can be understood by the observations below. During one iteration of the algorithm we pick a random position in  $A$ , but we keep it fixed until we test all values of  $D$ . If we change this position of  $A$  along one iteration we introduce spatial randomness and the algorithm does not converge. We also have to choose a single entry at each iteration; if we choose more than one entry to change at a time we introduce spatial randomness and the algorithm does not converge. The array  $D$  is just a repository of random phase values; we could say that we just pick  $N$  random phase values to test in  $A$  for each iteration of the algorithm. Therefore, if we choose a too small  $N$  the algorithm may not converge.

The experimental setup is shown in Fig. 2. A laser, model Ultralasers MSL-FN-532, of 200 mW and operating at 532 nm, is expanded and collimated by two confocal lenses  $L1$  and  $L2$ , of focal lengths  $f_1 = 8$  mm and  $f_2 = 125$  mm. The expanded beam forms a plane wave that uniformly illuminates a Holoeye LETO spatial light modulator (SLM), placed at the distance  $d = 540$  mm from the lens  $L3$ , of focal length  $f_3 = 1000$  mm. A computer-generated phase hologram (CGPH) utilized in the SLM is of type 3 [23], which contains the phase and amplitude of the calculated speckle field. The light reflected from the SLM is transformed to the Fourier plane

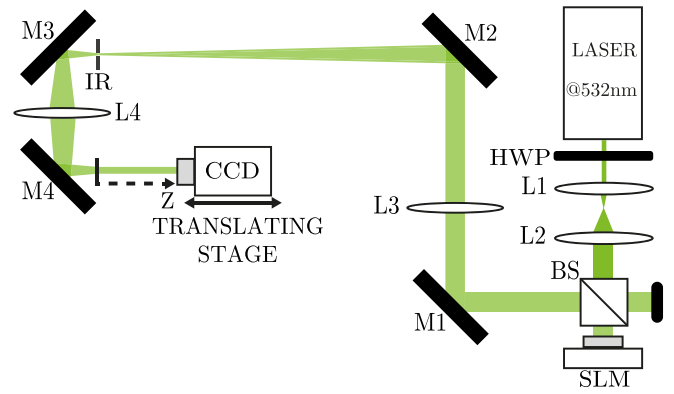


FIG. 2. Experimental setup: HWP is a half-wave plate;  $L1$ ,  $L2$ ,  $L3$ , and  $L4$  are lenses; BS is a beam-splitter; SLM is the spatial light modulator;  $M1$ ,  $M2$ ,  $M3$ , and  $M4$  are mirrors;  $A$  is a circular aperture; and CCD is a charge-coupled-device camera.

by the lens  $L3$ . The first diffraction order of this hologram is an intensity ring which is spatially filtered by an iris aperture  $IR$ . The lens  $L4$  of focal length  $f_4 = 150$  mm, confocal with  $L3$ , was used to image the ENRND speckles fields in a charge-coupled device (CCD) camera, which is mounted on a translating stage. Note that, to speed up the calculations, the number of pixels for the variables  $(x, y)$  should be a minimum value that still has a good resolution for displaying the speckle patterns. This is achieved by using  $300 \times 300$  pixels for the variables  $(x, y)$  in Eq. (2) for the optimization of all speckle patterns. Each speckle pattern is determined by the optimized values for the phase array  $\theta$ , which, actually gives the coefficients  $\Phi(\phi_n)$ , the only random terms in the plane wave expansion in Eq. (2). After optimization we just increase the number of pixels in the variables  $(x, y)$  to  $1080 \times 1080$  in the window size  $6.91$  mm  $\times$   $6.91$  mm that fits in the SLM. This process changes neither the contrast nor the shape of the patterns. For all patterns in this work we have used  $Q = 200$  and  $N = 150$ .

Figures 3(b) and 3(c) show experimental speckle patterns with contrasts in the super-Rayleigh regime. For comparison, in Fig. 3(a) is shown a standard Rayleigh speckle. These speckle patterns were measured in the image plane of the SLM and have  $k_r = 37.7$  mm $^{-1}$ . The value of  $k_r$  was the same for all experimental results in this work; it controls the spatial frequency of the speckles and affects the speckle grain size, but it does not affect the statistics. In the spatial Fourier domain the nondiffracting speckle fields transform to a ring whose radius is proportional to  $k_r$ . The Rayleigh speckle intensity profile with contrast ( $C = 1.01$ ) corresponds to the negative exponential PDF, the blue triangles in Fig. 3(d). The other speckle intensities profiles with  $C = 1.51$  and  $C = 1.80$  corresponds to the super-Rayleigh speckles with PDFs given by the green diamond and red squares, decaying slower than the Rayleigh speckles. Thereby, in the super-Rayleigh speckles, the light is concentrated in a few grains of speckles when compared with Rayleigh speckles.

Figure 4 shows results for an experimentally generated sub-Rayleigh speckle pattern. The speckle pattern in Fig. 4(a) also was captured in the image plane of the SLM. It has contrast,  $C = 0.78$ , that corresponds to the sub-Rayleigh statistics

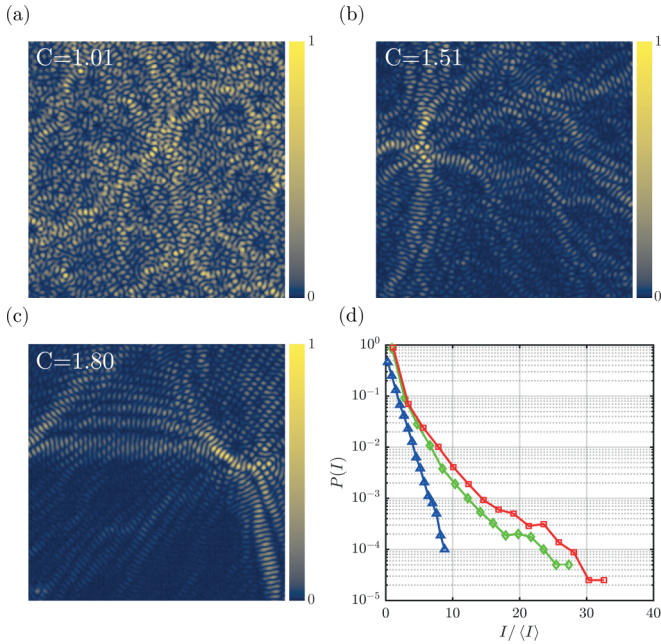


FIG. 3. Experimentally measured Rayleigh and super-Rayleigh speckles. (a) A standard Rayleigh speckle pattern. (b),(c) Super-Rayleigh speckle patterns. (d) The PDFs for the speckle patterns shown in this panel. In (a), (b), and (c) it was used a windows of  $0.7 \text{ mm} \times 0.7 \text{ mm}$  of the CCD camera.

for which the PDF is given by the green diamonds in Fig. 4(b). In the same figure a Rayleigh PDF is shown for comparison, with blue triangles. The sub-Rayleigh intensity distribution decays much faster than the negative exponential for the Rayleigh PDF. Because of the low contrast the grains of the speckle patterns are much closer so these patterns are more homogeneous. The combinations of low contrast and nondiffractive property may be useful in super-resolution microscopy [12] with infinite depth of focus.

Figure 5 illustrate experimental measurements of the transverse profile of ENRND speckle fields along the propagation. For each measurement, the ENRND speckle fields were propagated over ten Rayleigh ranges, where the Rayleigh range calculated in the experiment is  $R = 1.27 \text{ mm}$ . It can be noted

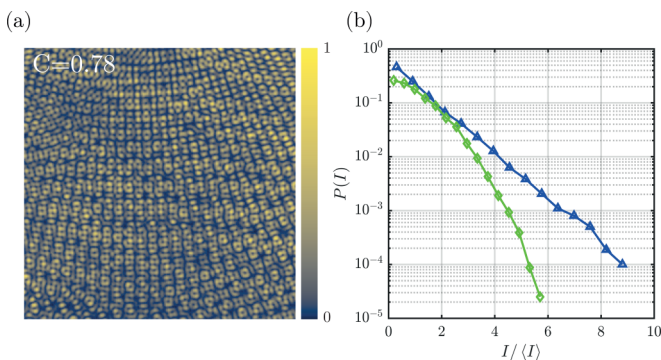


FIG. 4. Experimentally measured sub-Rayleigh speckles. (a) Sub-Rayleigh speckle pattern. (b) Comparison of the PDFs for the Sub-Rayleigh and Rayleigh speckle patterns. In (a) we used a windows of  $0.7 \text{ mm} \times 0.7 \text{ mm}$  of the CCD camera.

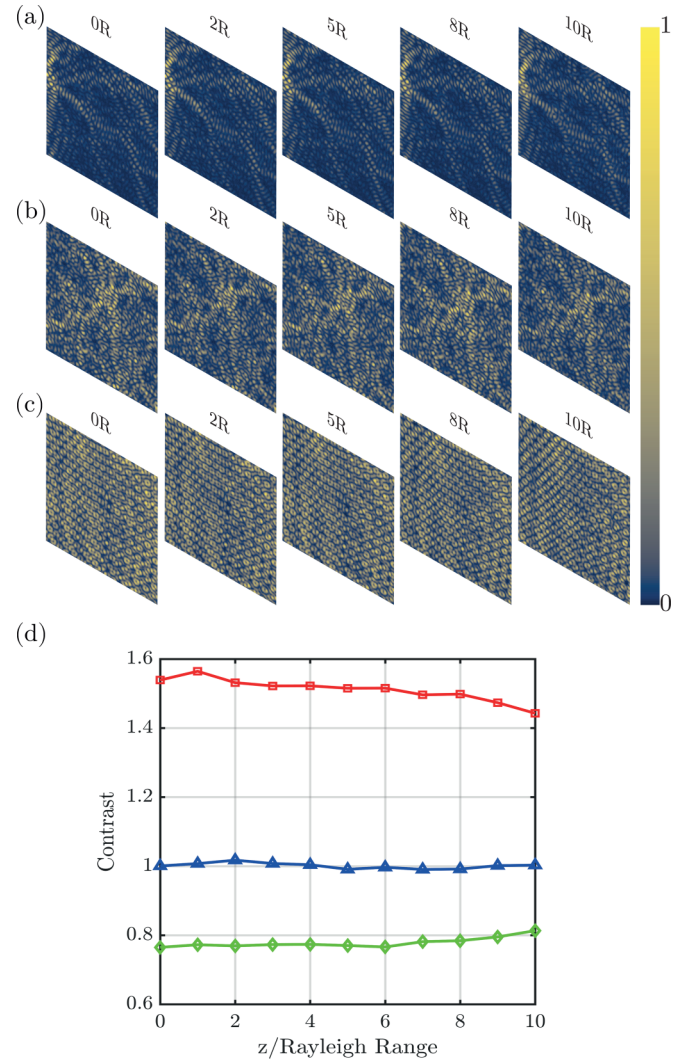


FIG. 5. Experimental measurement of speckles intensity profile along different axial positions corresponding to  $z = 0, 2, 5, 8,$  and  $10$  Rayleigh ranges: (a) Super-Rayleigh speckles with contrast ( $C = 1, 51$ ), (b) standard Rayleigh speckles with contrast ( $C = 1, 01$ ), and (c) sub-Rayleigh speckles with contrast ( $C = 0, 78$ ). All panels correspond to a windows of  $0.5 \text{ mm} \times 0.5 \text{ mm}$  of the CCD camera. In (d) we display the contrast along the axial propagation of Rayleigh speckles (blue triangles), sub-Rayleigh speckles (green diamonds), and super-Rayleigh speckles (red square). These curves are experimental data collected with the aid of a translation state.

that the intensity profile of the ENRND speckle fields stays almost the same during the propagated distance, i.e., it remains the image of the SLM in the initial Rayleigh position (0R). The first pattern in Fig. 5 at line (a) is a zoom of the Fig. 3(c), a super-Rayleigh pattern. The corresponding pattern in Fig. 5 at line (b) is a zoom of Fig. 3(a), a Rayleigh pattern. And the first pattern in Fig. 5 at line (c) is a zoom of Fig. 4(a), a sub-Rayleigh pattern. We keep this same zoomed region of interest along the propagation in Fig. 5. Figure 5(d) shows that the non-Rayleigh statistics exists for several Rayleigh ranges, as quantified through the contrast. It happens because Eq. (1) is an exact solution of the HE whose component plane waves extend to infinity and the spatial spectrum is limited to a



TABLE I. Numerical results for the second order correlations  $\Gamma_p^{(2)}$  at  $p$  different indexes.

	$\Gamma_1^{(2)}$	$\Gamma_2^{(2)}$	$\Gamma_3^{(2)}$	$\Gamma_4^{(2)}$
Rayleigh ( $C = 1$ )	0.0	2.0	0.0	0.0
Super-Rayleigh ( $C = 1.8$ )	0.0	2.0	0.0	2.1
Sub-Rayleigh ( $C = 0.8$ )	0.0	2.0	0.0	-0.3

circular slit of infinitesimally small width. Therefore, the field is a superposition of plane waves whose wave vectors lie in a cone, and for plane waves of infinite transversal length the transversal patterns do not change because each plane wave does not change, and neither do their relative phases change in this geometry [21]. But even in our experiment there is an approximation due to the spatial truncation of the constituent plane waves to fit in the SLM window.

To understand the origin of the non-Rayleigh statistics we proceed to analytically calculate the squared modulus of the space contrast  $C$  (see Appendix A),

$$C^2 = \frac{1}{Q^2} \sum_{n,n',m,m'} \langle e^{i[\theta(\phi_n) - \theta(\phi_{n'}) + \theta(\phi_m) - \theta(\phi_{m'})]} \rangle \times \delta_{n+m-n',m'} - 1, \quad (3)$$

where, for the numerical computation of Eq. (3), we have used  $Q = 200$ , the average in Eq. (3) was independently evaluated in an ensemble and spatially (see Appendix A),  $L = 11.96$  mm is the computational window, and  $k_t = 15.7$  mm<sup>-1</sup>. The sum in Eq. (3) is a sum over the second-order correlations between all the coefficients  $\Phi(\phi_n)$  of the plane wave superposition in Eq. (2). Similarly to Ref. [7], we can decompose this sum in four terms, corresponding to the second order correlations  $\Gamma_p^{(2)}$  at  $p$  different indexes, with  $p = 1, 2, 3$ , and 4, and the contrast can be written as  $C^2 = \Gamma_1^{(2)} + \Gamma_2^{(2)} + \Gamma_3^{(2)} + \Gamma_4^{(2)} - 1$ . For example,  $p = 4$  corresponds to

$$\Gamma_4^{(2)} = \frac{1}{Q^2} \sum_{n \neq n' \neq m \neq m'} \langle e^{i[\theta(\phi_n) - \theta(\phi_{n'}) + \theta(\phi_m) - \theta(\phi_{m'})]} \rangle \times \delta_{n+m-n',m'}.$$

Table I displays some contrast and correlations for different statistics and averaged over 100 patterns. It is clear that the non-Rayleigh statistics comes from the cross correlation corresponding to the summations over four different indexes in Eq. (3) [7].

We calculated the PDF of the phase  $\psi$  corresponding to the optimized  $\psi = \theta, A$ , or  $B$ , and for the sub-Rayleigh speckles, Fig. 6(a), or super-Rayleigh speckles, Fig. 6(c). It can be seen that they are all uniformly distributed even introducing the correlations at four different indexes observed in Table I. The ergodicity and stationarity are tested through the calculation of field cross-correlation  $|G_U(\Delta \mathbf{r})|^2$ , for the sub-Rayleigh speckles, Fig. 6(b), and super-Rayleigh speckles, Fig. 6(d). This cross-correlation is evaluated by a convolution between the speckle intensity and a spatially inverted version of itself, followed by a background subtraction [24]. The ergodicity is confirmed through the match of the calculated cross-correlation of a single patten and the average over 100

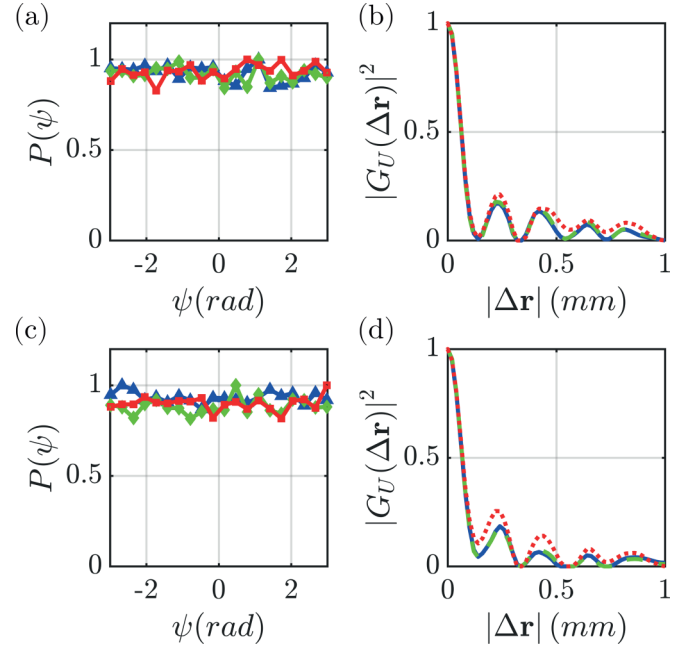


FIG. 6. Statistical properties of the optimized phases  $\psi = \theta, A$ , or  $B$ , and calculated speckle intensities. (a) Plot of the PDF of  $A$  (blue triangles), plot of the PDF of  $B$  (green diamonds), and plot of  $\theta$  (red squares) for sub-Rayleigh speckles, and (c) the same for super-Rayleigh speckles. (b) The speckle fields cross-correlations for sub-Rayleigh speckles for a one quarter of the calculated window and averaged over 100 patterns (green), for the full window averaged over 100 patterns (blue) and for a single pattern (red). (d) The same for super-Rayleigh speckles.

patterns. The stationarity is defined by the invariance of the cross-correlation by a spatial translation, which is equivalent to saying that the cross-correlation is the same for any selected area of the speckle pattern. Therefore, the stationarity is confirmed through the match between the field correlation over one quarter and over the full calculated area. The correlation length, roughly the full width at half maximum of the central peak of the cross-correlation [25], is the same for sub- and super-Rayleigh speckles. Figure 6 uses the same data used to obtain Table I.

In conclusion, we have discussed a method to generate ENRND speckles. This method relies on simple algorithm that aims to tailor higher-order correlations in the relative phase of a plane wave superposition that represents a non-diffractive speckle field. We have solved this problem using a naive algorithm which is usable in the present form, but future implementations can speed up the optimization procedure. The generated speckles are very general, and they can be directly tuned in a continuous range of contrast values, even in the sub-Rayleigh regime, preserving the nondiffractive property. These speckle fields may have applications in a broad range of areas, from condensed matter physics to optical imaging.

#### ACKNOWLEDGMENTS

This work was supported by Coordenação de Aperfeiçoamento de Pessoal e Nível Superior (CAPES), Conselho

Nacional de Desenvolvimento Científico e Tecnológico (CNPq), Fundação de Amparo Pesquisa do Estado de Alagoas (FAPEAL), and Instituto Nacional de Ciência e Tecnologia de Informação Quântica (INCT-IQ).

### APPENDIX A: THE CONTRAST AND THE CORRELATIONS BETWEEN RELATIVE RANDOM PHASES

Starting from the expression for the field,

$$U(x, y, z) = \frac{2\pi}{Q-1} e^{-ik_z z} \sum_n \Phi(\phi_n) e^{-ik_t(x \cos \phi_n + y \sin \phi_n)}, \quad (\text{A1})$$

where  $\phi_n = 2n\pi/(Q-1)$  and  $n = 0, \dots, Q-1$ , our goal is to write an expression for the contrast,

$$C^2 = \frac{\langle I^2 \rangle}{\langle I \rangle^2} - 1. \quad (\text{A2})$$

Therefore, we first calculate  $\langle I \rangle$ ,

$$\begin{aligned} \langle I \rangle &= \left( \frac{2\pi}{Q-1} \right)^2 \sum_{n, n'=0}^{Q-1} \langle \Phi(\phi_n) \Phi^*(\phi_{n'}) \rangle \langle e^{ik_t x (\cos \phi_{n'} - \cos \phi_n)} \rangle \\ &\quad \times \langle e^{ik_t y (\sin \phi_{n'} - \sin \phi_n)} \rangle. \end{aligned} \quad (\text{A3})$$

The only random function in Eq. (A3) is the function  $\Phi(\phi_n) = \exp[i\theta(\phi_n)]$ , where  $\theta(\phi_n)$  are the relative random phases of the plane waves superposition in Eq. (A1), therefore the average

$$\begin{aligned} \langle e^{ik_t x (\cos \phi_{n'} - \cos \phi_n)} \rangle &= \frac{1}{L} \int_{-L/2}^{+L/2} e^{ik_t x (\cos \phi_{n'} - \cos \phi_n)} dx \\ &= \frac{1}{k_t (\cos \phi_{n'} - \cos \phi_n) L} \\ &\quad \times 2 \sin \left[ k_t \frac{L}{2} (\cos \phi_{n'} - \cos \phi_n) \right], \end{aligned} \quad (\text{A4})$$

where  $L$  is the computational windows, is just a spatial average. Similar calculations are done for the average along the  $y$  coordinate in Eq. (A3). In the theoretical limit of an infinite window  $L \rightarrow \infty$ , applying L'Hôpital's rule, the result in Eq. (A4) is equal to 1 for  $n = n'$ , and oscillate infinitely fast for  $n \neq n'$ , resulting that the sum in Eq. (A3) is zero for  $n \neq n'$ . Besides, for  $n = n'$ ,  $\langle \Phi(\phi_n) \Phi^*(\phi_{n'}) \rangle = 1$ , therefore the average intensity is

$$\langle I \rangle = \left( \frac{2\pi}{Q-1} \right)^2 Q. \quad (\text{A5})$$

In fact, the results from the numerical calculation agrees with this reasoning.

In the following, we proceed to calculate  $\langle I^2 \rangle$ , obtaining

$$\begin{aligned} \langle I^2 \rangle &= \left( \frac{2\pi}{Q-1} \right)^4 \sum_{n, n', m, m'=0}^{Q-1} \langle \Phi(\phi_n) \Phi^*(\phi_{n'}) \Phi(\phi_m) \Phi^*(\phi_{m'}) \rangle \\ &\quad \times \langle e^{ik_t x (\cos \phi_{n'} - \cos \phi_n + \cos \phi_{m'} - \cos \phi_m)} \rangle \\ &\quad \times \langle e^{ik_t y (\sin \phi_{n'} - \sin \phi_n + \sin \phi_{m'} - \sin \phi_m)} \rangle. \end{aligned} \quad (\text{A6})$$

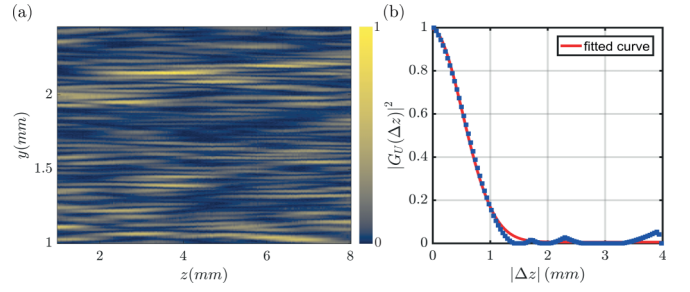


FIG. 7. (a) Longitudinal profile of diffractive speckles. (b) Axial cross-correlation function of the intensity pattern.

Following the same procedure used for the calculation of  $\langle I \rangle$  we can show that

$$\begin{aligned} \langle I^2 \rangle &= \left( \frac{2\pi}{Q-1} \right)^4 \sum_{n, n', m, m'=0}^{Q-1} \\ &\quad \times \langle e^{i[\theta(\phi_n) - \theta(\phi_{n'}) + \theta(\phi_m) - \theta(\phi_{m'})]} \rangle \delta_{n+m-n', m'}. \end{aligned} \quad (\text{A7})$$

Substituting Eqs. (A5) and (A7) in Eq. (A2), we obtain

$$C^2 = \frac{1}{Q^2} \sum_{n, n', m, m'=0}^{Q-1} \langle e^{i[\theta(\phi_n) - \theta(\phi_{n'}) + \theta(\phi_m) - \theta(\phi_{m'})]} \rangle \delta_{n+m-n', m'} - 1. \quad (\text{A8})$$

### APPENDIX B: MEASUREMENT OF THE RAYLEIGH RANGE

To measure the Rayleigh range, we used a diffractive speckle pattern with the same transversal coherence length as the used sub- and super-Rayleigh nondiffractive speckles. We measured intensity patterns for 200 axial positions along propagation starting from the initial position corresponding to the image plane of SLM. After that we took a line of pixels along the center of each measured pattern and concatenated them to form Fig. 7(a), a longitudinal intensity profile. We calculated the intensity cross-correlation function of each horizontal line of pixels in Fig. 7(a) and averaged over all lines to obtain the result in Fig. 7(b), which is the axial intensity cross-correlation function, and its full width at half maximum

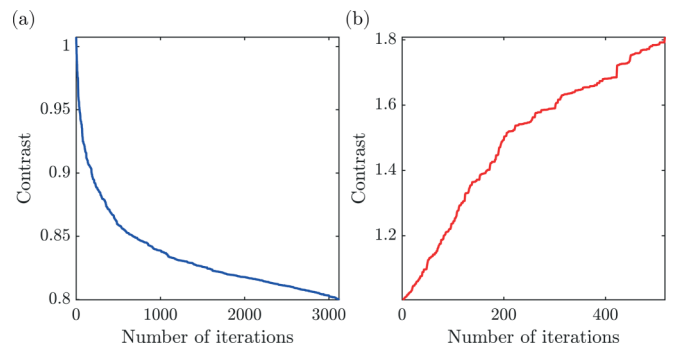


FIG. 8. Evolution of the contrast along the optimization for (a) sub-Rayleigh (b) super-Rayleigh speckles.

gives the longitudinal length of a single speckle grain defined as the Rayleigh range  $R = 1.27$  mm [9].

### APPENDIX C: CONVERGENCE OF THE PROPOSED ALGORITHM

In order to better understand how the algorithm evolves along the optimization process, one typical example is shown

in Fig. 8. The graph shows the contrast after each iteration of the algorithm. We observe that the algorithm has a uniform convergence and that the convergence for the sub-Rayleigh speckles is slower than for the super-Rayleigh speckles. We also note that, at least, any contrast between the maximum and the minimum value displayed in Fig. 8 can be obtained.

- 
- [1] J. Goodman, *Speckle Phenomena in Optics: Theory and Applications* (Roberts & Company, Greenwood Village, CO, 2007).
- [2] C. R. Alves, A. J. Jesus-Silva, and E. J. Fonseca, Self-reconfiguration of a speckle pattern, *Opt. Lett.* **39**, 6320 (2014).
- [3] F. O. Fahrbach, P. Simon, and A. Rohrbach, Microscopy with self-reconstructing beams, *Nat. Photonics* **4**, 780 (2010).
- [4] F. O. Fahrbach and A. Rohrbach, Propagation stability of self-reconstructing Bessel beams enables contrast-enhanced imaging in thick media, *Nat. Commun.* **3**, 632 (2012).
- [5] J. Durnin, J. J. Durnin, Jr., and J. H. Eberly, Diffraction-Free Beams, *Phys. Rev. Lett.* **58**, 1499 (1987).
- [6] D. G. Pires, A. F. Sonsin, A. J. Jesus-Silva, and E. J. Fonseca, Three-dimensional speckle light self-healing-based imaging system, *Sci. Rep.* **8**, 563 (2018).
- [7] Y. Bromberg and H. Cao, Generating Non-Rayleigh Speckles with Tailored Intensity Statistics, *Phys. Rev. Lett.* **112**, 213904 (2014).
- [8] J. a. P. Amaral, E. J. S. Fonseca, and A. J. Jesus-Silva, Tailoring speckles with Weibull intensity statistics, *Phys. Rev. A* **92**, 063851 (2015).
- [9] N. Bender, H. Yılmaz, Y. Bromberg, and H. Cao, Customizing speckle intensity statistics, *Optica* **5**, 595 (2018).
- [10] N. Bender, H. Yılmaz, Y. Bromberg, and H. Cao, Creating and controlling complex light, *APL Photonics* **4**, 110806 (2019).
- [11] L. Mandel and E. Wolf, *Optical Coherence and Quantum Optics* (Cambridge University Press, Cambridge, 1995).
- [12] N. Bender, M. Sun, H. Yılmaz, J. Bewersdorf, and H. Cao, Circumventing the optical diffraction limit with customized speckles, *Optica* **8**, 122 (2021).
- [13] K. Kuplicki and K. W. C. Chan, High-order ghost imaging using non-Rayleigh speckle sources, *Opt. Express* **24**, 26766 (2016).
- [14] E.-F. Zhang, W.-T. Liu, and P.-X. Chen, Ghost imaging with non-negative exponential speckle patterns, *J. Opt.* **17**, 085602 (2015).
- [15] R. Liu, B. Qing, S. Zhao, P. Zhang, H. Gao, S. Chen, and F. Li, Generation of Non-Rayleigh Nondiffracting Speckles, *Phys. Rev. Lett.* **127**, 180601 (2021).
- [16] J. Durnin, Exact solutions for nondiffracting beams. I. the scalar theory, *J. Opt. Soc. Am. A* **4**, 651 (1987).
- [17] J.-C. Garreau, Quantum simulation of disordered systems with cold atoms, *C. R. Phys.* **18**, 31 (2017).
- [18] A. S. Nunes, S. K. Velu, I. Kasianiuk, D. Kasyanyuk, A. Callegari, G. Volpe, M. M. T. da Gama, G. Volpe, and N. A. Araújo, Ordering of binary colloidal crystals by random potentials, *Soft Matter* **16**, 4267 (2020).
- [19] T. Schwartz, G. Bartal, S. Fishman, and M. Segev, Transport and anderson localization in disordered two-dimensional photonic lattices, *Nature (London)* **446**, 52 (2007).
- [20] G. N. Watson and E. T. Whittaker, *A Course of Modern Analysis*, *Cambridge Mathematical Library* (Cambridge University Press, Cambridge, 1996).
- [21] O. C. Vicente and C. Caloz, Bessel beams: a unified and extended perspective, *Optica* **8**, 451 (2021).
- [22] J. P. Amaral, J. C. Rocha, E. J. Fonseca, and A. J. Jesus-Silva, Method to define non-diffracting optical beams mimicking the shape of simple plane curves, *Appl. Opt.* **58**, 3659 (2019).
- [23] V. Arrizón, U. Ruiz, R. Carrada, and L. A. González, Pixelated phase computer holograms for the accurate encoding of scalar complex fields, *J. Opt. Soc. Am. A* **24**, 3500 (2007).
- [24] A. J. Jesus-Silva, J. G. Silva, C. H. Monken, and E. J. S. Fonseca, Experimental cancellation of aberrations in intensity correlation in classical optics, *Phys. Rev. A* **97**, 013832 (2018).
- [25] C. R. Alves, J. P. Amaral, A. P. Neto, J. G. Neto, and A. J. Jesus-Silva, Measuring the topological charge of coherence vortices through the geometry of the far-field cross-correlation function, *Appl. Opt.* **59**, 1553 (2020).